Differences of characteristics and performance with Bi3+ and Bi2O3 doping over TiO2 for photocatalytic oxidation under visible light

Article

Accepted Version

It is advisable to refer to the publisher's version if you intend to cite from the work. See Guidance on citing.

Differences of characteristics and performance with Bi^{3+} and Bi_2O_3 doping over TiO_2 for photocatalytic oxidation under visible light

Qiong Huang[1, *], Juan Ye[1], Han Si[1], Bo Yang[1], Tao Tao[1], Yunxia Zhao[1], Mindong Chen[1] and Hong Yang[1, 2, *]

[1] Jiangsu Collaborative Innovation Center of Atmospheric Environment and Equipment Technologies, Jiangsu Key Laboratory of Atmospheric Environmental Monitoring & Pollution Control, School of Environmental Science & Engineering, Nanjing University of Information Science & Technology, Nanjing 210044, China;

[2] Department of Geography and Environmental Science, University of Reading, Whiteknights, Reading, RG6 6AB, UK

*Corresponding author 1: Dr. Qiong Huang

School of Environmental Science and Engineering, Nanjing University of Information Science & Technology, Nanjing 210044, China

Address: No. 219 Ningliu Road, Nanjing University of Information Science & Technology, School of Environmental Science and Engineering, 210044, Nanjing, China

E–mail: hqhaixia@163.com (Q.H.)

Tel: +86 25 58731090   Fax: +86 25 58731090

*Corresponding author 2: Dr. Hong Yang

Department of Geography and Environmental Science, University of Reading, Whiteknights, Reading, RG6 6AB, UK

E–mail: hongyanghy@gmail.com (H. Y.)

Tel: +44 (0)1183787750

Differences of characteristics and performance with Bi^{3+} and Bi_2O_3 doping over TiO_2 for photocatalytic oxidation under visible light

Abstracts: Bi-doped TiO_2 photocatalysts were synthesized by sol with a high-pressure hydrothermal method and developed for the photocatalytic degradation of formaldehyde under the visible light irradiation and ambient temperature. According to characterization, it could be found that some Bi-doped TiO_2 could be transformed into the distinctive crystals phase of $Bi_4Ti_3O_{12}$, which was crucial for improving activity. The excess Bi_2O_3 doping into TiO_2, such as Bi_2O_3-N/TiO_2 and Bi_2O_3-C/TiO_2, generated a mixed oxides with Bi_2O_3 and $Bi_4Ti_3O_{12}$, was not beneficial to increase the activity of HCHO oxidation, whereas Bi^{3+}/TiO_2 composed of TiO_2 and $Bi_4Ti_3O_{12}$ displayed a higher activity with good stability. It was worth noteworthy that Bi^{3+}/TiO_2 didn't show the lowest binding energy. However, it exhibited a lower PL intensity, higher adsorption, and activity due to the uniform particulates, high surface areas, and the strong interaction between TiO_2 and $Bi_4Ti_3O_{12}$, attributing to create superoxide radical anion ($^{\bullet}O_2^{-}$) and hydroxyl radical ($\bullet OH$). The present results of Bi^{3+}/TiO_2 indicated that HCHO could be effectively oxidized from 1.094 to 0.058 mg/m^3 (94.7%) under visible light irradiation within 36 h. The current research made effort to draw out the existing state of Bi, which would be better, Bi^{3+} or Bi_2O_3, doped in the TiO_2.

Keywords: TiO_2; Bi-doped; Photocatalytic oxidation; Formaldehyde; Visible light

1. Introduction

With the rapid development of economy and urbanization, decoration has turn into a kind of popular lifestyle. A large number of new decorative materials and furniture have been used in rooms, while they can release a variety of volatile organic compounds (VOCs), such as formaldehyde [1, 2], benzene [3, 4], toluene [5, 6] and so on [7]. Accordingly, indoor air pollution has become an increasingly serious problem. As people spend more time indoors than outdoors, people may suffer from a serious of greater impact on human health, including nausea, dizzy, headache, leukemia, and even cancer [8]. In particular, formaldehyde (HCHO), one of the notorious carcinogenic and deformity-causing substances identified by the World Health Organization (WHO), has been detected at elevated levels in various indoor environments [9]. Hence, seeking an effective method to remove indoor HCHO has been an urgent task. To date, the main strategies of eliminating HCHO include adsorption [10], photocatalysis [11, 12], low temperature plasma [13], and catalytic oxidation at ambient temperature [14]. Considering efficiency and practicality, photocatalytic oxidation using TiO_2 semiconductors is one of advanced technologies and it is still receiving attentions from many researches [15, 16]. Up to now, TiO_2 is still the most frequently used photocatalyst due to the high solar sensitivity, chemical stability and low toxicity [17]. In addition, its high density of states in bands enables the efficient photo to current conversion, and this makes TiO_2 more active than other semiconductors, such as ZnO, SnO_2, ZrO_2, CdS and g-C_3N_4 [18]. Therefore, TiO_2 has been widely applied in various photocatalytic fields, such as water and gas stream treatment, and organic contaminant decomposition [19, 20]. However, owing to its large band gap energy of 3.2 eV ($\lambda < 380nm$), TiO_2 absorbs only ultraviolet light rather than more visible light that including a large part of solar irradiation [21, 22]. Furthermore, the overall quantum yield rate can be seriously impacted by the low electron transfer rate and a high recombination rate of photo-induced electrons and holes. In order to overcome those problems, lots of efforts have been made to adjust the properties of TiO_2 with electronic, for example, the noble metal deposition [22], the other semiconductor coupling [23], and metal cations or non-metal anions doping [24-27]. Coupling of TiO_2 with Bi_2O_3 [28], as a promising semiconductor, has been found to be a

82 good strategy for elongating the light region to the visible and enhancing the

83 photocatalytic activity [29]. Bi_2O_3 is an excellent material for the photocatalytic

84 oxidation due to its narrow band gap of 2.8 eV and diversity in crystal structure with

85 doping of TiO_2. Some studies about the Bi_2O_3/TiO_2 composite or Bi-doped TiO_2 found

86 better performance of VOCs photocatalytic oxidation under the excitation of visible

87 light [30]. However, it is still unclear about the existence state of bismuth to improve the

88 oxidation activity over Bi-doped TiO_2, especially for Bi^{3+} or Bi_2O_3, which donate as

89 composite oxides (Bi_xTiO_y), or mixed oxides (Bi_2O_3-TiO_2), separately. Murcia-Lopez

90 et al. [31] synthesized a series of Bi^{3+}-doped TiO_2 catalysts with 2wt% doping to evaluate

91 the photocatalytic oxidation of phenol under UV–vis illumination and they found that

92 the nominal content of Bi^{3+} in TiO_2 was the main reason for the increase in the

93 photocatalytic activity. Bentouami et al. [32] also found that the binding energy of Bi

94 detected by XPS wasn't the same as the one of Bi in Bi_2O_3, and the shift in binding

95 energies of XPS could be ascribed to some valence states higher than Bi^{3+}. Bouattour

96 et al. [33] and Xu et al. [34] suggested that the doped Bi ions substitute some of the

97 titanium atoms in the form of compound oxidation, such as Ti-O-Bi, $Sr_{1-x}Bi_xTi_{1-x}Fe_xO_3$,

98 and $BiFeO_3$, according to the results of XRD and XPS. Kang et al [35] found that Bi ions

99 inserted into TiO_2 could markedly improve CO_2 reduction to CH_4 due to the inhibited

100 recombination of photogenerated electron-hole. However, some scholars had a different

101 opinion that Bi_2O_3 rather than Bi^{3+} played an important role in the photocatalytic

102 oxidation over Bi-doped TiO_2. For instance, Li et al. [36] found that the flower-like

103 Bi_2O_3/TiO_2 with enrichment Bi_2O_3 quantum dots on the surface of photocatalyst

104 exhibited higher activity due to the strong interaction between Bi_2O_3 and TiO_2. Leung

105 [37] and Wang [38] et al. hold that heterojunction structures with mixed semiconductors,

106 such as $TiO_2/ZnO/Bi_2O_3$, 3D $BiOCl_xBr_{1-x}$/graphene oxide, could effectively improve

107 the separation efficiency of photogenerated electron/hole and increase the subsequent

108 photocatalytic activity. Meanwhile, some researcher suggested that bismuth might

109 coexist in the form of Bi^{3+} and Bi_2O_3 over Bi-doped TiO_2 photocatalysts. Li et al. [39]

110 reported an ordinary approach, doping Bi_2O_3 powder into TiO_2 sol, to synthesis Bi-

111 doped TiO_2 photocatalyst. When the loading of Bi_2O_3 exceed 5mol%, $Bi_2Ti_4O_{11}$ phase

112 started to appear and showed a good crystallization. The calcination temperature had a

113 key effect on the chemical state of Bi, a direct effect on the photocatalytic activity.

114 Attributed to the synergetic effect of Bi_xTiO_y and TiO_2, the photocatalytic activity over

115 Bi-doped TiO_2 could be improved. Gao et al. [30] found that $Bi_4Ti_3O_{12}$ and Fe-doped

116 $Bi_4Ti_3O_{12}$ nanosheets, described with a formula of $(Bi_2O_2)^{2+}(Bi_2Ti_3O_{10})^{2-}$, which was

117 constructed with a TiO_6 octahedral and a $(Bi_2O_2)^{2+}$ monolayer, displayed a high

118 photocatalytic oxidation of bisphenol A and phenol, although not as good as Au-2%Fe/

119 $Bi_4Ti_3O_{12}$ composite photocatalysts. According to the XPS analysis, XPS signals of

120 Bi_2O_3 powders could also be found. Prabhakaran et al. [40] reported that Bi-doped and Bi–

121 N co-doped TiO_2 nanocomposites could exhibit preferable photocatalytic activities for

122 fabric dye under visible light illumination. However, the results of XRD were different

123 from the results of XPS. XRD spectra showed crystalline Bi_2O_3, while the positive shift

124 of XPS peaks corresponding to $Bi4f_{7/2}$ and $Bi4f_{5/2}$ might also be ascribed to Bi-O-Ti

125 bonds formation on the photocatalyst surface.

126 To summarize, it is still difficult to clarify the state of Bi, as composite oxides or mixed

127 oxides, for obtaining a high activity over Bi-doped TiO_2 photocatalysts. I t is still

128 necessary to investigate the state of Bi in-depth and find the rules between bismuth and

129 TiO_2 in Bi-doped TiO_2 with composite oxides or mixed oxides. The most attractive

130 aspect of these photocatalysts is the synergistic combination of bismuth oxide and

131 titanium oxide, as doped Bi ions substitute titanium atoms in the form of compound

132 oxidation or doped Bi_2O_3 with TiO_2 in the form of heterojunction structure. Different

133 from previous studies that some simple approaches have been developed to synthesize

134 Bi-doped TiO_2 photocatalysts with the formation of Bi_xTiO_y or Bi_2O_3-TiO_2, bismuth

135 and titanium oxide with composite oxides or mixed oxides were produced for

136 photocatalytic oxidation of low concentration of HCHO under visible light irradiation

137 in this study. The possible mechanism of photocatalytic activities of Bi_xTiO_y and Bi_2O_3-

138 TiO_2 was discussed. This research provides a better understanding of the different

139 composite oxides or mixed oxides in the process of photocatalytic oxidation of HCHO.

140 **2. Materials and Methods**

141 *2.1. Syntheses of photocatalysts*

142 All reagents, such as ethanol, glycerol and acetic acid, were analytical grade and were

143 used without further purification in the experiments. For comparison, three different

144 types of Bi-doped TiO_2 photocatalysts were prepared.

145 The first one was for Bi^{3+}/TiO_2 as composite oxides. 14.3 mL tetrabutyl titanate was

146 added into 8.5 mL ethanol and 8.5 mL glycerol in a conical flask, denoted as solution

147 A with a constant magnetic stirring. 3.2 g bismuth nitrate $(Bi(NO_3)_3 \cdot 5H_2O)$ and 0.4 g

148 ammonium carbonate $((NH_4)_2CO_3)$ were dissolved into 8.5 mL ethanol, 8.5 mL

149 glycerol and 6.6 mL acetic acid, denoted as solution B with the magnetic mixture. Later,

150 the solution B dropped into solution A with constant agitation. The resulting solution

151 was stirred for 30 min and transfer into a stainless steel reactor for 2 days aging at 110

152 ^oC. Finally, the precipitate was centrifuged and scrubbed with using distilled water and

153 ethanol for three times, and then dried at 80 ^oC for 2.5 h and calcined at 450 ^oC for 8.5h

154 [41].

155 The second were for Bi_2O_3-C/TiO_2 and Bi_2O_3-N/TiO_2 as composite/mixed oxides. 3.2

156 g bismuth nitrate $(Bi(NO_3)_3 \cdot 5H_2O)$ was added into 100 mL distilled water with

157 magnetic stirred until complete dissolution. 30 mL of 4M NaOH aqueous solution was

158 dropped until the pH at 12. With a continuous stirring for 12 h, the suspension was

159 centrifuged and washed with distilled water twice, and then dried at 60 ^oC and calcined

160 at 450 ^oC for 4h, denoted as Bi_2O_3-C powders, or not calcined at 450 ^oC for 4h, denoted

161 as Bi_2O_3-N powders, to obtain two different powders (Bi_2O_3-C and Bi_2O_3-N). After that,

162 another solution was prepared with the same way as Bi^{3+}/TiO_2 without bismuth nitrate,

163 and then these Bi_2O_3-C or Bi_2O_3-N powders were added into the mixed solution

164 together under constant agitation. After that, the resulting solution was stirred for 30

165 min and transfer into a stainless steel reactor for 2 days aging at 110 ^oC. Finally, the

166 precipitate was centrifuged and scrubbed with using distilled water and ethanol for three

167 times, and then dried at 80 ^oC for 2.5 h and calcined at 450 ^oC for 8.5h. These catalysts

168 were identified as Bi_2O_3-C/TiO_2 and Bi_2O_3-N/TiO_2.

169 The third one was for $Bi_2O_3-TiO_2$ as mixed oxides. Two types of powders, such as

170 Bi_2O_3-N and TiO_2, were synthesized in the same way as above. And then, these two

171 kinds of Bi_2O_3-N and TiO_2 powders were mixed with mechanical blending, confirmed

172   as Bi_2O_3-TiO_2.

173   *2.2. Characterization*

174   The crystal structures of three different styles of photocatalysts were all detected by

175   using a D/max-RB X-ray diffractometer (XRD, D8 Advance, Bruker, Germany)

176   equipped with Cu Kα radiation (λ = 0.15406 nm) in a 2θ range of 10-80° and the

177   scanning speed was 4°/min. Raman spectra were measurement on Renishaw inVia

178   Raman systems at ambient temperature and fitted with the 532 nm line of an Ar ion

179   laser as an excitation source. The microscopic morphological structure and particle size

180   of these prepared samples were observed by using a scanning electron microscope

181   (SEM, Hitachi S-4800, Hitachi, Japan) and a transmission electron microscope (TEM,

182   JEM-2100, JEOL, Japan). The Brunauer-Emmett-Teller (BET, ASAP-2020,

183   Micromeritics Instrument Corporation, USA) surface areas of the spent catalysts and

184   pre-treated were determined by using nitrogen adsorption at 77.3 K. The UV-vis spectra

185   (UV-vis, Lambda 950, Perkin-Elmer, USA) of samples were recorded with an

186   integrating sphere attachment. The scanning range was between 250 nm and 800 nm,

187   and $BaSO_4$ was used as a reference. The excited states of these catalysts composite were

188   detected with photoluminescence (PL, MicOS, HORIBA Scientific, USA). In-situ

189   diffuse reflectance infrared transform spectrometry (DRIFTS, Nicolet 6700FTIR,

190   Thermo, USA) was carried out on a spectrometer fitted with a MCT detector and a high-

191   temperature reaction chamber, which could supply all the necessary gas inlets or outlets

192   and allow for measuring and controlling the temperature. The spectra could be acquired

193   with an accumulation of 64 scans and a resolution of 4 cm^{-1}. IR spectra (Nicolet 410

194   FTIR, Thermo, USA) on KBr pellets of the samples were recorded on a spectrometer

195   at a resolution of 4 cm^{-1}. The concentration of the samples in KBr was maintained at

196   approximately 0.3%. The X-ray photoelectron spectroscopy (XPS, AXIS ULTRA DLD,

197   Shimadzu-Krotos, Japan) spectra were obtained by using an AlKα X-ray source (1486.6

198   eV) operated at 15 kV and 300 W with an ESCALAB250 Thermo VG to understand

199   the chemical binding energies of the Bi, Ti and O. Electron paramagnetic resonance

200   (EPR, JES-FA200, JEOL, Japan) spectra was collected from a spectrometer with

201   employing an X-band microwave frequency (9.43GHz) and power (1.5mW) at room

202 temperature.

203 *2.3. Activity evaluation of HCHO removal*

204 The photocatalytic degradation of HCHO over Bi-doped TiO_2 catalysts was carried out

205 in a self-designed glass reactor ($600\times600\times600$ mm). 1mL HCHO (38wt%) was dropped

206 into a petri dish and removed into this glass reactor for five minutes. When the

207 concentration was 1.05 ± 0.05 mg/m^3, the petri dish was moved out and another petri

208 dish with 0.4g photocatalyst powder was transferred into the glass reactor quickly. After

209 that, the glass reactor was immediately sealed by using a glass cover with vaseline.

210 Through a small hole in the front of the glass reactor, the concentration of formaldehyde

211 was detected by using a formaldehyde meter (PPM-400st, PPM Technology, UK),

212 which designed to measure HCHO concentrations from 0 to 24.56 mg/m^3 in snatch

213 samples of air. A 36W energy-saving lamp (LED) providing the visible light was fixed

214 10cm above the catalyst. When the concentration became stable and the adsorption-

215 desorption equilibrium remained, the energy-saving lamp was turned on and HCHO

216 concentration was measured using the PPM-400st meter for three times at every 12 h.

217 To investigate the photocatalytic activity of different catalysts, a set of gaseous

218 experiments were carried out in the indoor environment.

219 **3. Results and discussion**

220 *3.1 The activity of Bi-doped TiO_2 for HCHO oxidation*

221 Fig. 1 shows the conversion of HCHO and stability under visible light irradiation over

222 different types of Bi-doped TiO_2 photocatalysts as a function of time. The conditions in

223 standard tests were composed of HCHO concentration (1.05 ± 0.05 mg/m^3), reaction

224 temperature (20-30°C), LED type (36 W) and catalyst powder (0.40 g). In terms of the

225 blank and adsorption tests over TiO_2, Bi_2O_3 and Bi^{3+}/TiO_2 catalysts under dark, the

226 concentration of HCHO decreased from 1.052 to 0.923 mg/m^3 at 48h in the blank (Fig.

227 1 (A)), indicating that the glass reactor owned good airtightness without HCHO leakage.

228 Although the Bi^{3+}/TiO_2 photocatalysts exhibited better adsorption than TiO_2 and Bi_2O_3,

229 the adsorption amount of HCHO was still very low, even negligible. In terms of the

230 photocatalytic activity and stability over these Bi-doped TiO_2 catalysts, the

231 photocatalytic activity and stability of Bi^{3+}/TiO_2 were significantly higher than other

232   three kinds of Bi-doped TiO_2 catalysts due to the composition and structure (Fig. 1(B)

233   and (C)). The HCHO concentration decreased from 1.094 to 0.058 mg/m^3 at 36h, even

234   below the limits value of standard (0.08 mg/m^3). Moreover, the catalyst demonstrated

235   good stability with four consecutive tests. However, Bi_2O_3-N/TiO_2, Bi_2O_3-C/TiO_2, and

236   Bi_2O_3-TiO_2 catalysts showed the same activity for HCHO degradation and the

237   conversion was about 50% at 48h. Meanwhile, the stability of Bi_2O_3-N/TiO_2 was as bad

238   as its oxidation activity, without improving. Owing to the rapid recombination of

239   photogenerated electrons and holes, although Bi_2O_3 owned lower band gap energy (2.9

240   eV) than TiO_2 (3.2 eV), it exhibited the lowest activity for HCHO oxidation.

241

242

243
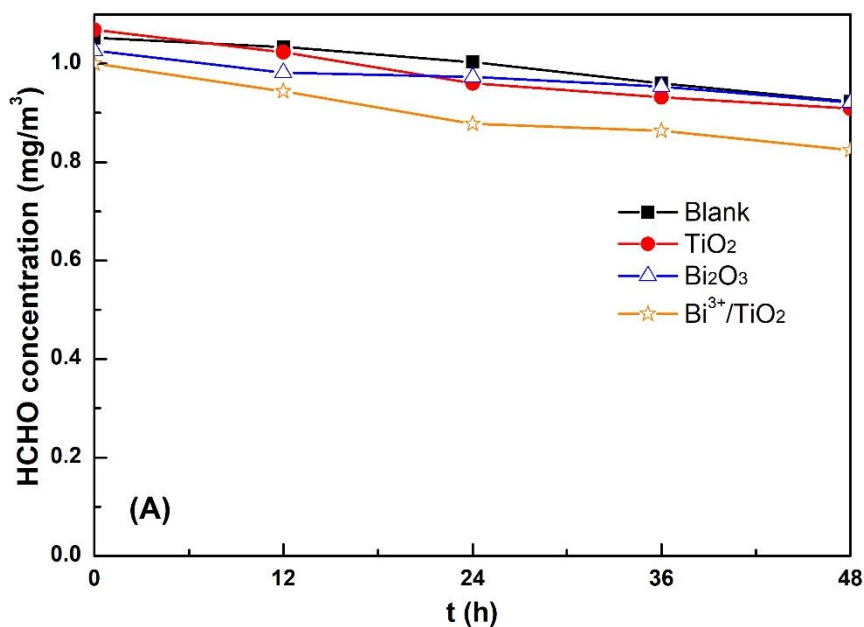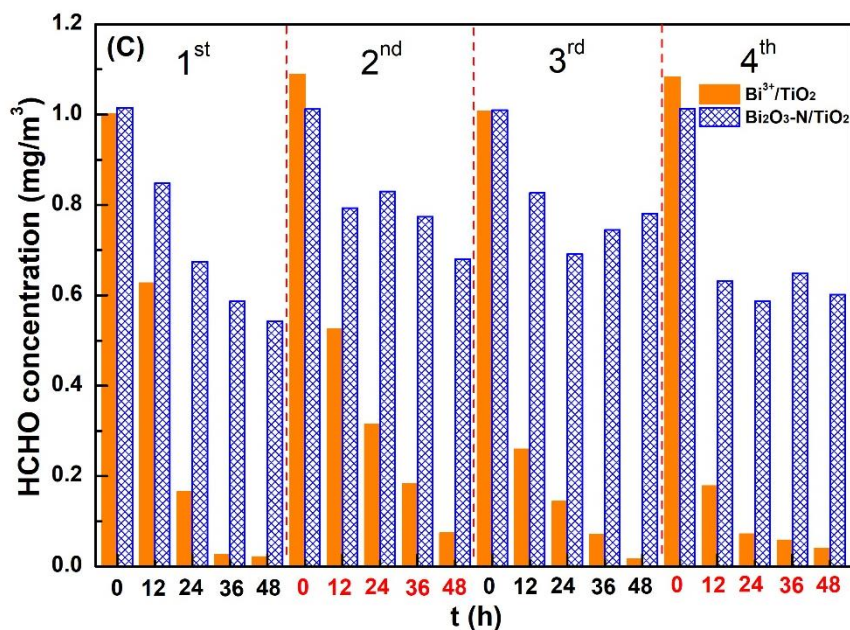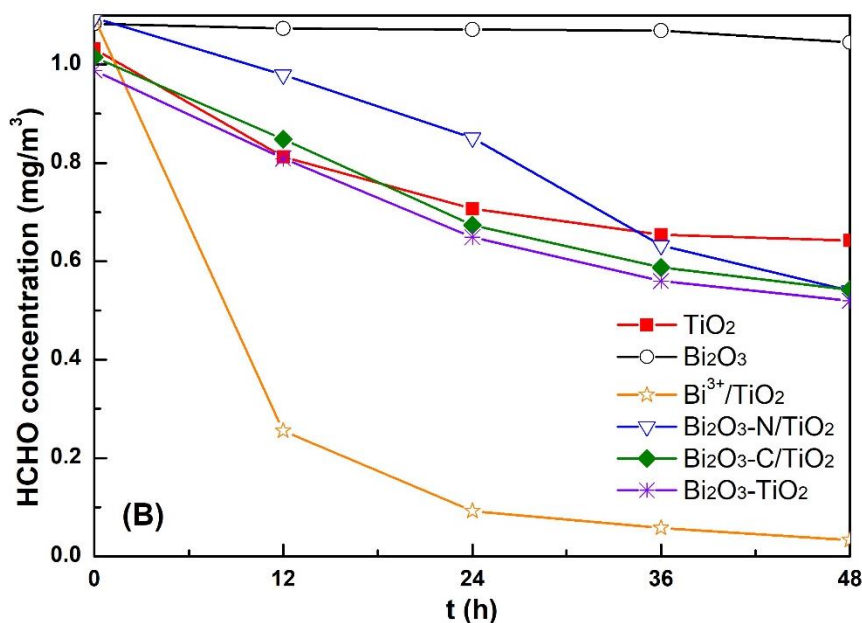
Fig. 1. Photocatalytic degradation of HCHO and stability over Bi-doped TiO_2 catalysts (A: blank and adsorption experiments under dark; B: photocatalytic oxidation of HCHO over Bi-doped TiO_2 catalysts; C: stability experiments over Bi^{3+}/TiO_2 and Bi_2O_3-N/TiO_2 with four times)

3.2 XRD analysis

Fig. 2 shows the XRD patterns of Bi-doped TiO_2 catalysts with different preparation methods calcinated at 450 ^{o}C for 8.5 h. For comparison, the XRD patterns of the as-prepared pure Bi_2O_3 and TiO_2 were also provided. The XRD patterns of TiO_2 and Bi_2O_3 were corresponded to the anatase phase of TiO_2 (PDF # 21-1272) and the monoclinic phase of α-Bi_2O_3 (PDF # 41-1449), respectively. Both of them showed good crystal

253 structures with the sharp diffraction peaks accompanied by calcinating at 450 $^{\circ}$C for 8.5

254 h and the crystal peaks were calculated by using the Scherrer equation attributed to (1

255 0 1) and (1 2 0) planes to be 11.9 nm and 84.3 nm. In terms of Bi-doped TiO_2 catalysts,

256 except for Bi_2O_3-TiO_2 mixed oxides, the XRD patterns of Bi^{3+}/TiO_2 were assigned to

257 anatase TiO_2 and a new characteristic peak at 30.2° and 33.1° ascribed to the composite

258 oxide of $Bi_4Ti_3O_{12}$ (PDF # 35-0795). Regarding Bi_2O_3-N/TiO_2 and Bi_2O_3-C/TiO_2

259 catalysts, the XRD patterns displayed almost the same diffraction peaks indexed to the

260 monoclinic phase of α-Bi_2O_3 and the composite oxide of $Bi_4Ti_3O_{12}$, implying that Bi_2O_3

261 with calcining or not had no effect on the crystal structure. This is due to that these two

262 kinds of Bi-doped TiO_2 catalysts composed of Bi_2O_3 and $Bi_4Ti_3O_{12}$ led to a lower

263 activity than Bi^{3+}/TiO_2. In terms of Bi_2O_3-TiO_2 mixed oxide catalyst, the diffraction

264 peaks in the patterns were ascribed to the TiO_2 and α-Bi_2O_3, respectively. Therefore,

265 the above results indicated that the heterojunction structure with TiO_2 and $Bi_4Ti_3O_{12}$

266 was the critical factor to obtain a high activity for HCHO oxidation, rather than the

267 incorporation of Bi_2O_3 and $Bi_4Ti_3O_{12}$, even with Bi_2O_3 and TiO_2.

268
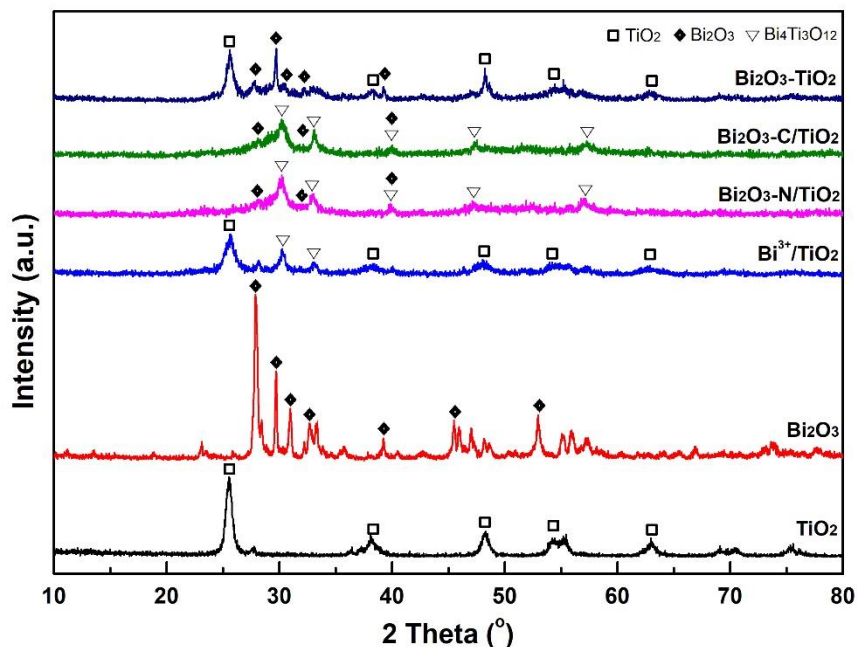
269 Fig. 2. XRD patterns of TiO_2, Bi_2O_3, and Bi-doped TiO_2 catalysts

270

271

272 *3.3 BET analysis*

Table 1. Textural properties of TiO_2, Bi_2O_3, and Bi-doped TiO_2 catalysts

Samples	S_{BET} (m²/g)	V_p (cm³/g)	d_p (nm)
TiO_2	59.53	0.11	5.76
Bi_2O_3	37.96	0.03	5.43
Bi^{3+}/TiO_2	52.39	0.12	7.82
Bi_2O_3-N/TiO_2	27.3	0.07	6.73
Bi_2O_3-C/TiO_2	42.78	0.10	7.23
$Bi_2O_3-TiO_2$	50.51	0.11	6.67
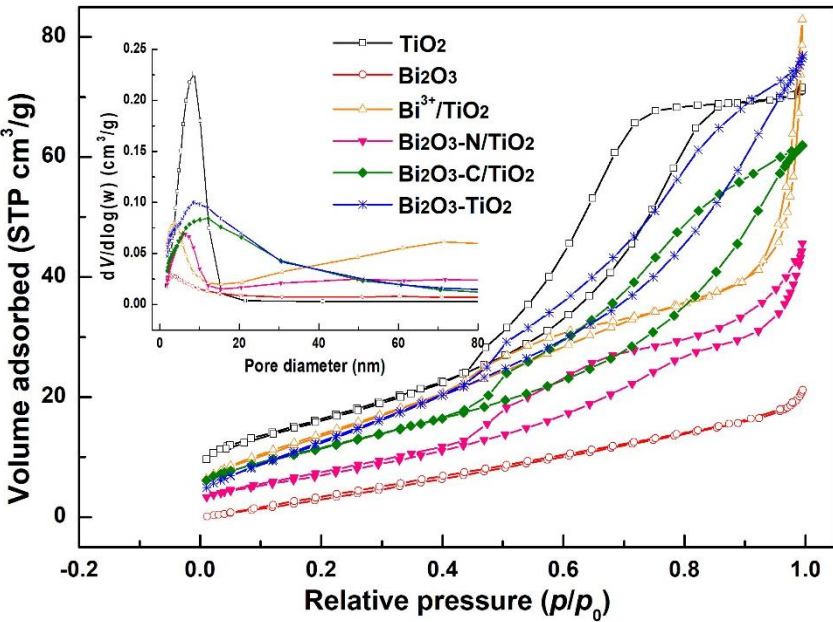
Fig. 3. Nitrogen adsorption-desorption isotherms and pore-size distribution curves of TiO_2, Bi_2O_3, and Bi-doped TiO_2 catalysts

In general, the large surface areas of catalysts can provide more active sites to adsorbent reactant molecules and then oxidize, which can effectively improve the activity of HCHO oxidation. Fig. 3 shows N_2 adsorption-desorption isotherms and the appropriate pore size distribution curves of different types of Bi-doped TiO_2 catalysts. The isotherms of TiO_2 displayed a type IV isotherm with a H2 hysteresis loops, which may include typical "ink bottle" holes, tubular holes with uneven pore size distribution, or densely packed spherical particle interstitial holes, etc. Bi-doped TiO_2 catalysts, except for Bi^{3+}/TiO_2, showed adsorption-desorption isotherms of type IV with an overlap of H2 and H3 hysteresis loops, resulting from bottle-ink and slit-like pores, signifying that the pore sizes of these samples lied in the range of 2–50 nm. The result could also be

287 confirmed by the pore size distribution and the result of BET (Table 1) and SEM (Fig.

288 5), which demonstrated that the pore sizes of these samples were from 5 to 8 nm.

289 However, Bi^{3+}/TiO_2 displayed two distinct hysteresis loops, implying that one of the

290 hysteresis loops was the channel in these particles and the other should be the

291 accumulation hole of the particles. The result implied that Bi^{3+}/TiO_2 had larger channels,

292 which was also confirmed by the pore size distribution and the improved HCHO

293 adsorption. Bi^{3+}/TiO_2 (S_{BET}=52.39 m^2/g) exhibited the largest surface areas and pore

294 sizes among these different types of Bi-doped TiO_2 catalysts. In addition, the surface

295 areas of TiO_2 and Bi_2O_3 were calculated to be 59.53 m^2/g and 37.96 m^2/g, respectively.

296 Bi_2O_3 and Bi_2O_3-N/TiO_2 exhibited extremely low pore volume, which were aligned

297 with the adsorption-desorption isotherms, and these could significantly decrease the

298 adsorption of HCHO and be detrimental for the improvement of oxidation activity.

299 Therefore, the above results demonstrated that the specific surface areas maybe not the

300 most important factor for photocatalytic oxidation of HCHO, but it could display a

301 minor role in the activity enhancement.

302 *3.4 Raman analysis*

303
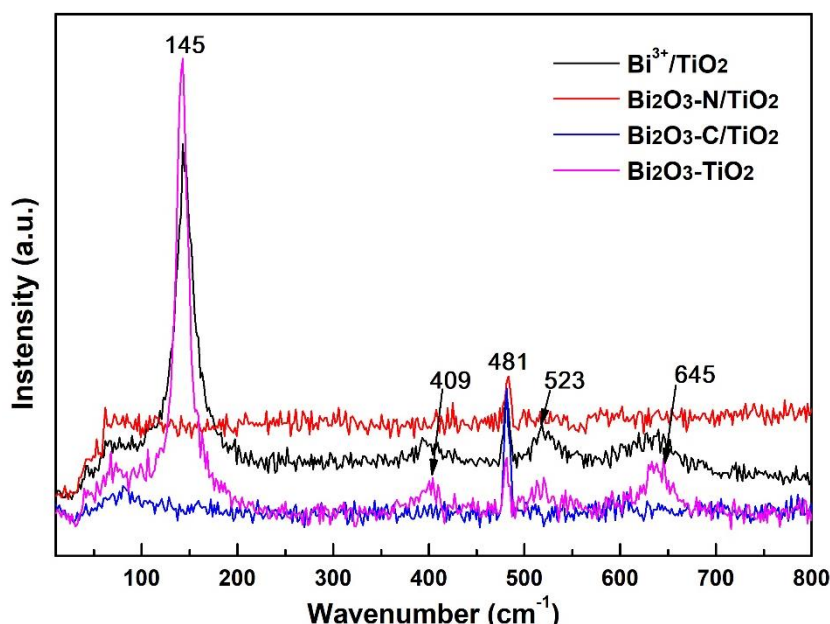
304 Fig. 4. Raman spectra of Bi-doped TiO_2 catalysts

305 Fig. 4 shows the Raman spectra of Bi-doped catalysts with different synthetic methods.

306 The peaks at 145, 409, 523 and 645 cm^{-1} could be identified to the characteristic bands

307 of anatase TiO_2 [39], indicating that the TiO_2 was one of the main phase structures in the

308 sample of Bi^{3+}/TiO_2 and Bi_2O_3-TiO_2, which was consistent with the XRD results. While

309 for Bi_2O_3-N/TiO_2 and Bi_2O_3-C/TiO_2, it was difficult to detect the presence of anatase

310 TiO_2 by Raman spectra. More importantly, the Raman peak at 481 cm^{-1} could be

311 assigned to the characteristic band of Bi_2O_3. Among these samples, the Bi_2O_3-C/TiO_2

312 exhibited the strongest intensity due to Bi_2O_3 powder calcined at 450 ^{o}C for 4h. While

313 for Bi_2O_3-N/TiO_2, Bi_2O_3-C/TiO_2 and Bi^{3+}/TiO_2, it was easy to find the presence of

314 $Bi_4Ti_3O_{12}$, not Bi_2O_3, by the XRD measurement, which was not corroborate well with

315 Raman spectra. That was because the composite oxides of $Bi_4Ti_3O_{12}$ contained the

316 characteristic band of Bi_2O_3.

317 *3.5 Morphology measurement*

318 The morphology structure of TiO_2, Bi_2O_3, and Bi-doped TiO_2 catalysts were

319 investigated by using SEM and TEM. TiO_2 showed an aggregated of lumpy particles

320 with a smooth surface, while Bi_2O_3 displayed some aggregated and smaller particles

321 with a rough surface attributed to nano-sized spherical Bi_2O_3 (Fig. 5(B)). Bi_2O_3-TiO_2

322 (Fig. 5(C)) mixed oxides with TiO_2 and Bi_2O_3 exhibited the same image as the images

323 of Fig. 5(A) and Fig. 5(B) without changing. Regarding Bi-doped TiO_2 catalysts (Fig.

324 5(D-F)), SEM image of Bi^{3+}/TiO_2 composites that were composed of mutually

325 aggregated spherical nanoparticles showed a uniform particulate state and it could

326 improve the adsorption of visible light and HCHO to increase the activity. While,

327 samples of Bi_2O_3-N/TiO_2 and Bi_2O_3-C/TiO_2 calcined at 450 ^{o}C for 8.5h displayed

328 irregular and smooth-surfaced lumps, indicated that there was a melting-

329 recrystallization-remelting process for these composites. As can be seen in Fig. 5(G),

330 the observed lattice spacing of 0.234 nm was attributed to the (0 14 0) crystal planes of

331 $Bi_4Ti_3O_4$, and lattice spacing of 0.243 nm and 0.166 nm (not shown) corresponded to

332 the (1 0 3) and (2 1 1) crystal planes of anatase TiO_2, respectively. However, the images

333 of Bi_2O_3-N/TiO_2 and Bi_2O_3-C/TiO_2 catalysts exhibited that these particles aggregated

334 together and produced a large number of lumps with a smooth surface due to roasted

335 Bi_2O_3 without doping into TiO_2. According to Fig. 5(H), the lattice spacing of 0.234

336 nm, 0.271 nm, 0.269 nm and 0.256 nm matched well with the (0 14 0) crystal planes of

337 $Bi_4Ti_3O_4$ and the (-1 2 2), (2 2 0), and (-2 1 2) crystal planes of Bi_2O_3 (not shown). The

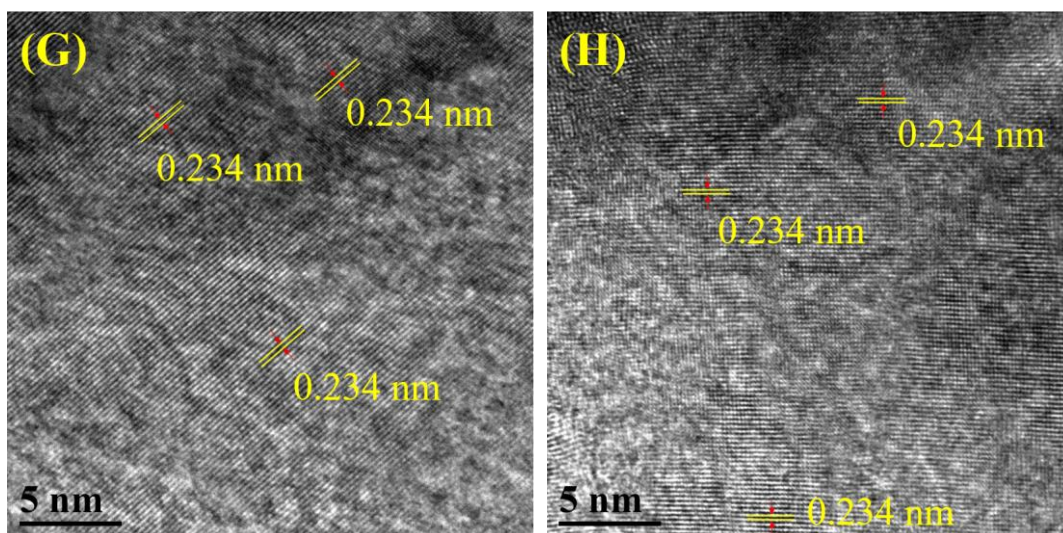338 above results were all in accordance with the XRD exhibited in Fig. 2.

339

340

341

342
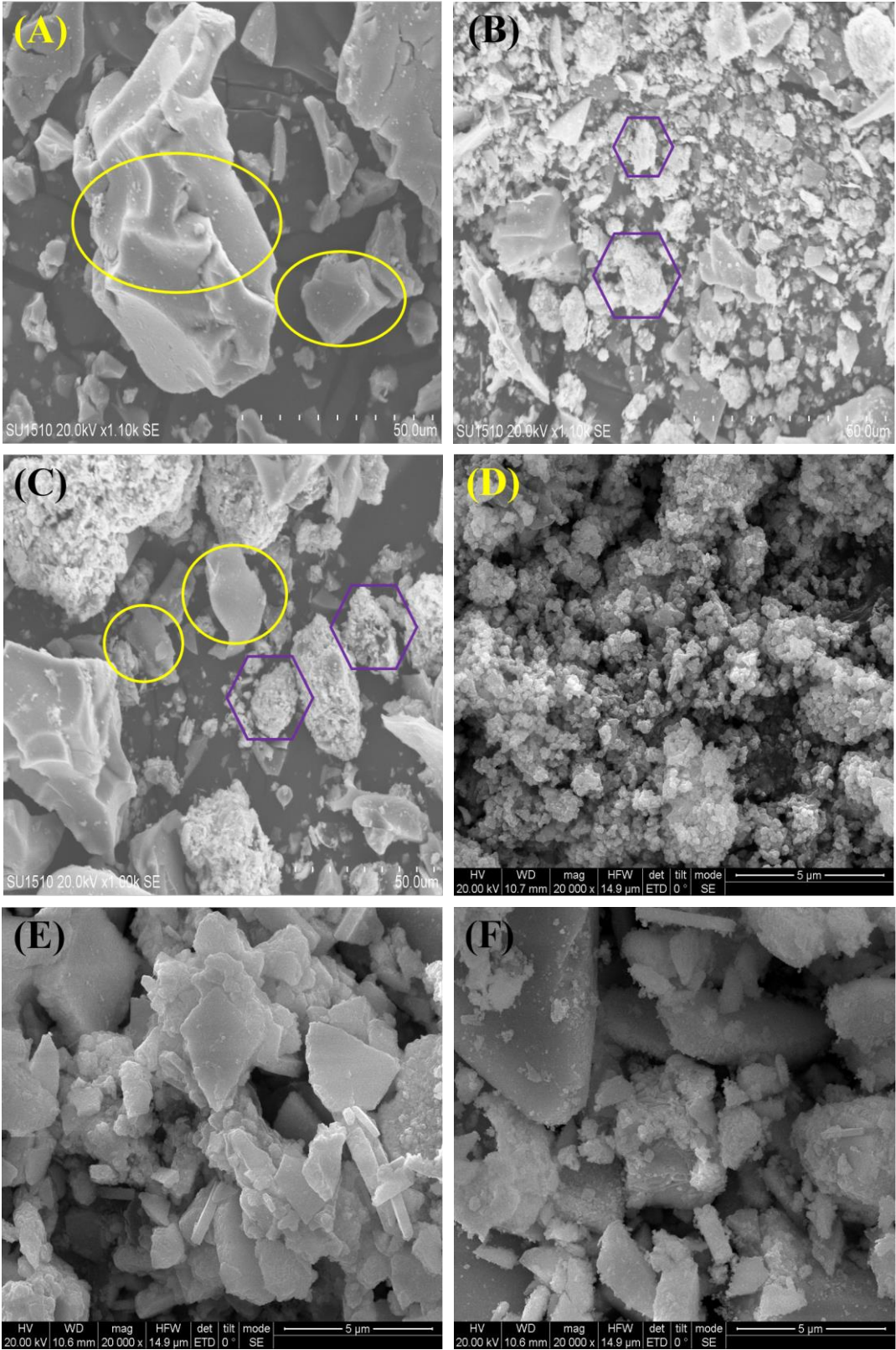
Fig. 5 SEM and TEM images of photocatalysts: (A) TiO_2, (B) Bi_2O_3, (C) Bi_2O_3-TiO_2, (D, G) Bi^{3+}/TiO_2, (E, H) Bi_2O_3-N/TiO_2, and (F) Bi_2O_3-C/TiO_2

3.6 Optical absorption properties

The corresponding UV-vis DRS and PL spectra of TiO_2, Bi_2O_3 and Bi-doped TiO_2 catalysts are presented in Fig. 6. The absorption peak of pure TiO_2 at 380–780 nm could be found as anatase TiO_2 and the band gap energy (E_g) was 3.1 eV, which displayed visible light absorption and low E_g (3.2 eV) due to the incorporation of N or C with $(NH_4)_2CO_3$. The absorption intensities of Bi_2O_3 with the E_g of approximately 2.9 eV in the visible region from 380 to 450 nm were markedly higher than those in other visible regions. Bi_2O_3 displayed visible light absorption and low E_g, and it exhibited the worse activity than other samples due to the rapid recombination of photogenerated e^- and h^+. Therefore, Bi_2O_3 couldn't be used independently as an oxide catalyst for HCHO oxidation and it needed to be combined with other semiconductors, such as TiO_2, to form heterojunctions structure or others to improve the oxidation activity. In terms of Bi-doped TiO_2 samples, Bi^{3+}/TiO_2 with the E_g of around 3.0 eV exhibited the highest absorption at UV and visible regions, so it showed the highest activity for HCHO degradation at ambient temperature. Bi_2O_3-N/TiO_2 and Bi_2O_3-C/TiO_2 displayed almost the same visible light absorption and E_g (2.8 eV) owing to the rapid recombination of photogenerated e^- and h^+ with Bi_2O_3. Therefore, the samples of Bi_2O_3-N/TiO_2 and Bi_2O_3-C/TiO_2 displayed poor activities for HCHO oxidation. The above results were all consistent with the activity of Bi-doped TiO_2 for HCHO oxidation.

364   The PL spectra were designed to evaluate the excited state of photocatalysts and the

365   recombination rate of photoinduced e^- and h^+. In this study, the excitation wavelength

366   was 325 nm at room temperature and examined in the range of 350-900 nm with a

367   single scan mode. Fig. 6(C) shows the PL spectra of Bi_2O_3-N/TiO_2, Bi_2O_3-C/TiO_2,

368   Bi^{3+}/TiO_2 and Bi_2O_3-TiO_2. Among these four samples, Bi_2O_3-C/TiO_2 exhibited the

369   highest PL intensity, indicating that Bi_2O_3-C/TiO_2 showed a high recombination rate of

370   photoinduced e^- and h^+, which was not beneficial to increase the activity for

371   photocatalytic oxidation of HCHO. While, compared with Bi_2O_3-N/TiO_2, Bi^{3+}/TiO_2

372   displayed a lower PL intensity, implying that Bi^{3+}/TiO_2 could improve charge

373   separation with a low recombination rate of e^- and h^+. This was mainly due to the Bi^{3+}

374   doping on TiO_2, which can capture photogenerated e^- from the surface of $Bi_4Ti_3O_{12}$ to

375   reduce charge recombination. This result indicates that Bi^{3+}/TiO_2 can exhibit a higher

376   photocatalytic activity due to that Bi^{3+} doping TiO_2 hinders free carriers from

377   recombination under irradiation. Although Bi_2O_3-TiO_2 showed the lowest PL intensity,

378   the photocatalysts of Bi_2O_3 composite was not conducive to photocatalytic oxidation of

379   HCHO. The above results show that the critical factor to determine the activity of these

380   photocatalysts was Bi^{3+}/TiO_2 that was composed of TiO_2 and $Bi_4Ti_3O_{12}$, confirmed by

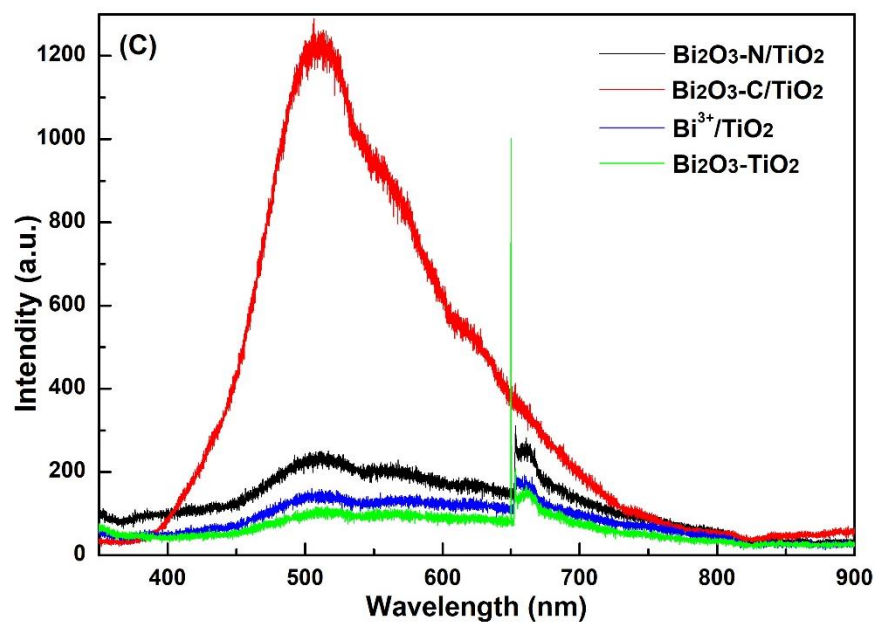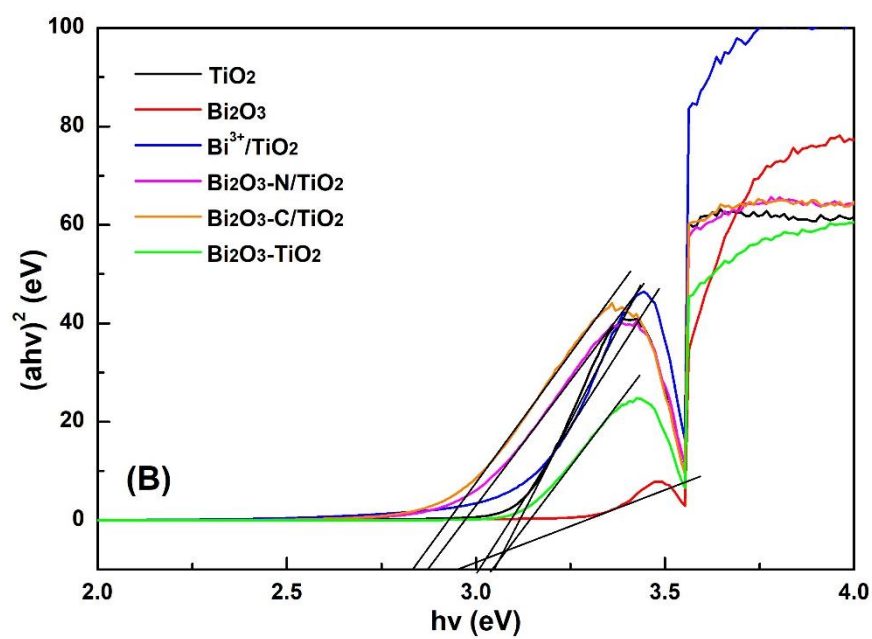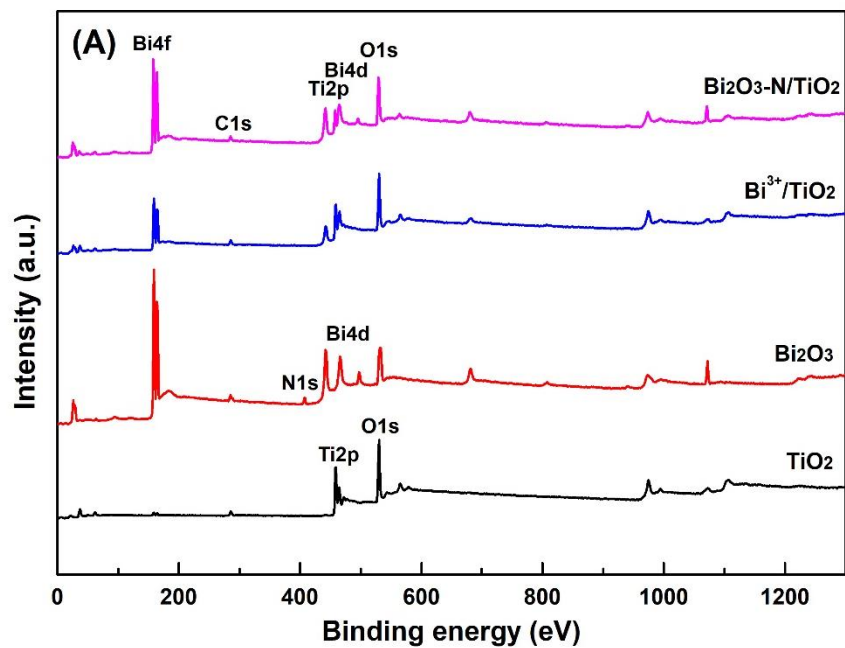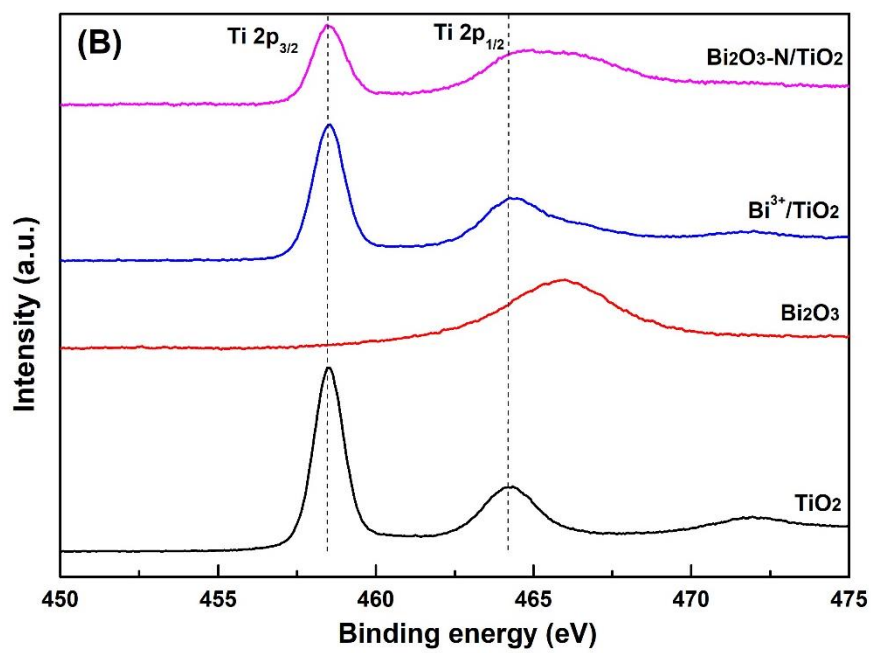381   XRD.

382

383

384
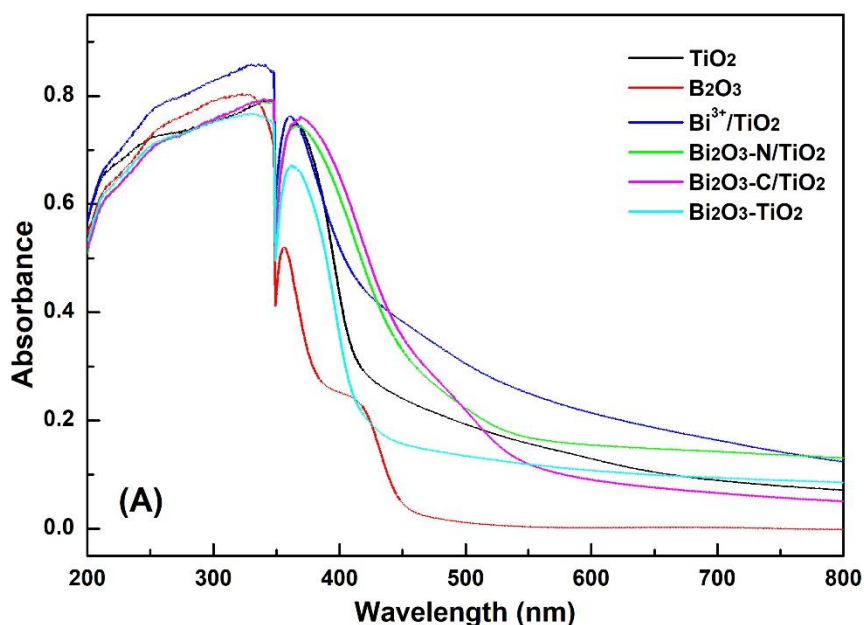
385   Fig. 6. Diffuse reflectance UV-vis and PL spectra of TiO_2, Bi_2O_3, and Bi-doped TiO_2 catalysts
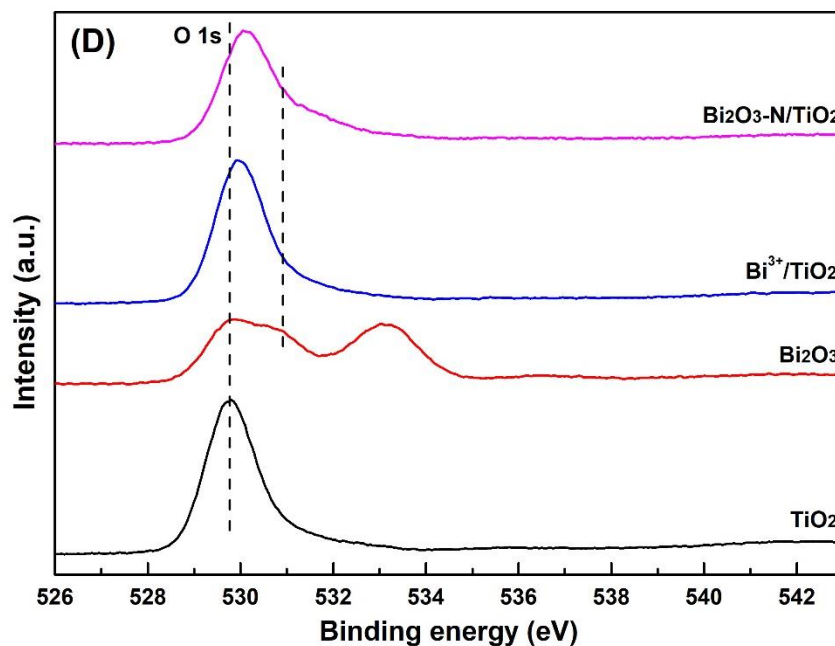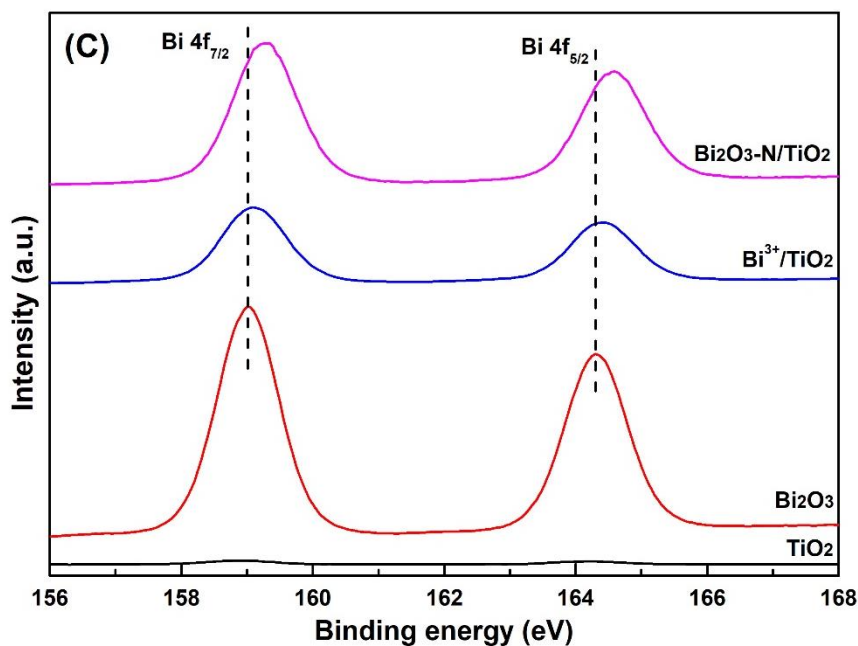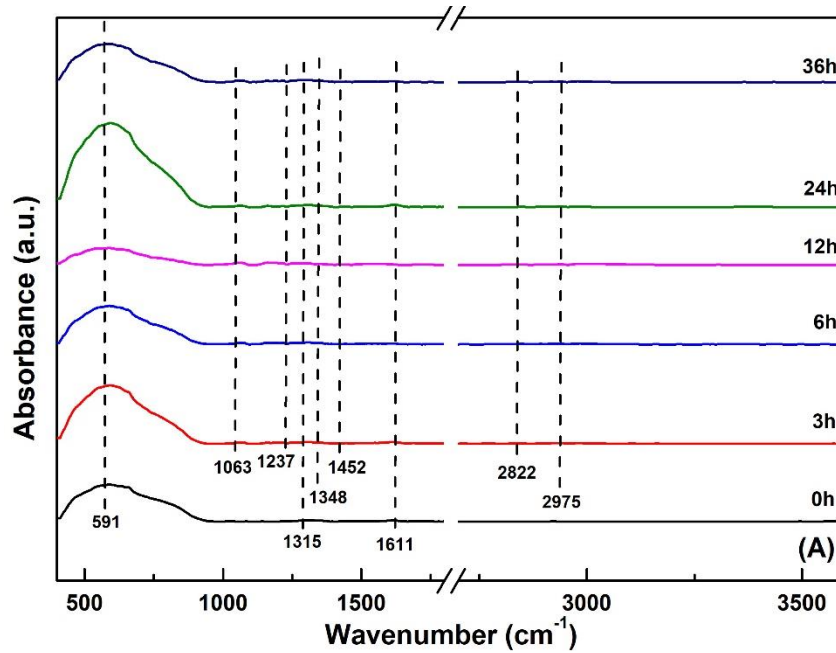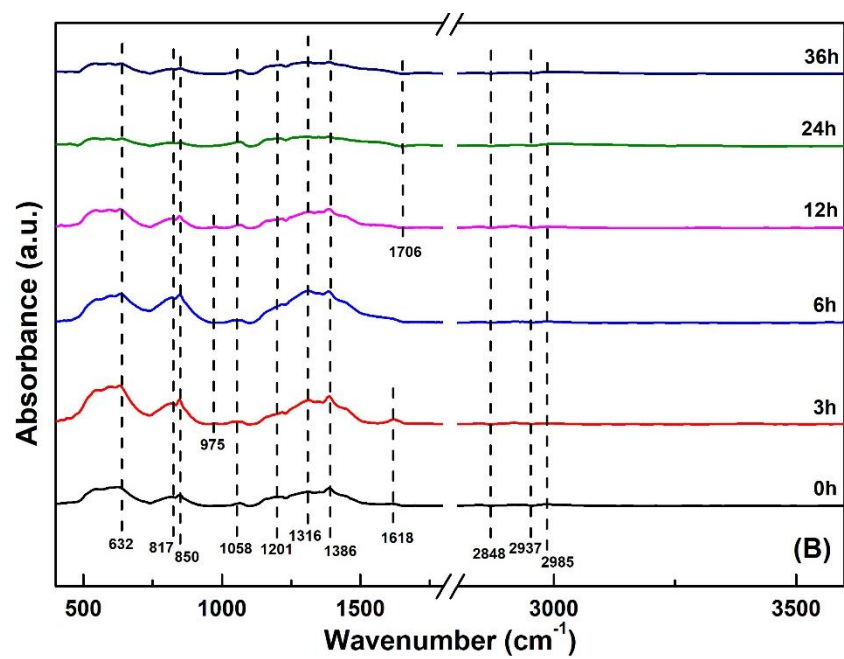
386   *3.7 XPS analysis*

387

388

389

390

391   Fig. 7. XPS spectra of different types of TiO_2, Bi_2O_3, and Bi-doped TiO_2 catalysts

392 The chemical states of TiO_2, Bi_2O_3, and Bi-doped TiO_2 catalysts were detected by using

393 XPS analysis. Ti, Bi, O, C and N elements could be observed on the surface of samples

394 (Fig. 7). The Ti $2p_{3/2}$ and T $2p_{1/2}$ for TiO_2 and Bi^{3+}/TiO_2 were situated at a binding

395 energy (BE) of 458.5 eV and 464.2 eV, respectively. However, the BE of T $2p_{1/2}$ for

396 Bi_2O_3-N/TiO_2 was shifted to high binding energy due to the influence of Bi_2O_3 [39]. The

397 results implied that Bi^{3+}/TiO_2 and Bi_2O_3-N/TiO_2 consisted of TiO_2 and Bi_2O_3, and these

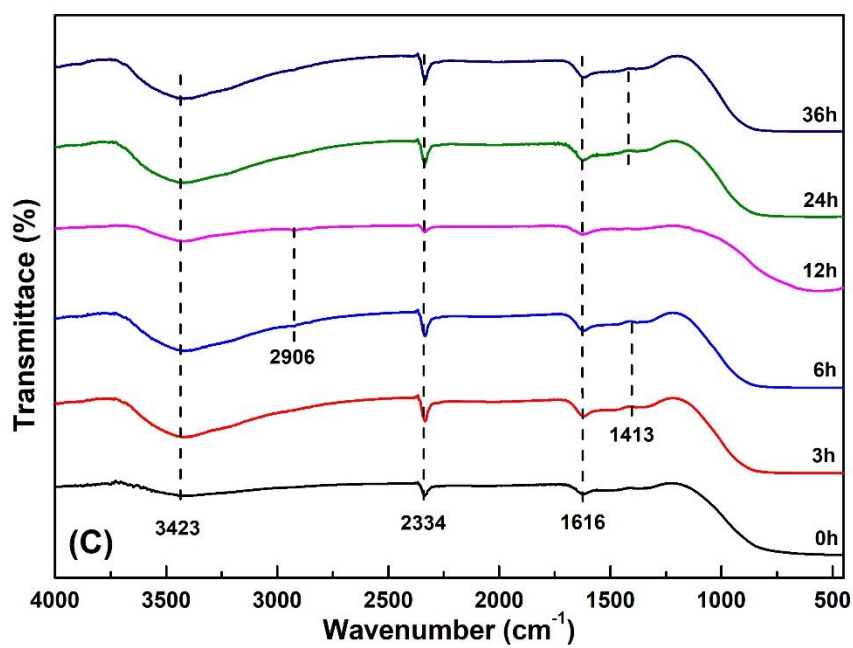398 were all consistent with XRD analysis. Interestingly, the Bi 4f photoelectron peaks of

399　Bi-doped TiO_2 had a positive shift to a high BE with pure Bi_2O_3, indicating that the

400　introduction of Bi could induce a strong interplay and　e^- transferred between TiO_2 and

401　Bi_2O_3 to generate composite oxides ($Bi_4Ti_3O_{12}$). Among them, Bi_2O_3-N/TiO_2 was the

402　most obvious and Bi^{3+}/TiO_2 was the second, and the result was in agreement with UV-

403　vis and PL spectra. The XPS of the O 1s were also detected. The O 1s levels for TiO_2

404　and Bi_2O_3 were markedly different and fell to 529.8 eV and 533.1 eV, respectively. In

405　general, the O 1s could be deconvoluted into three contributions [7]: one with the BE of

406　529.8-529.3 eV indicated to lattice oxygen (O_{lat}), and the other two with BE of 531.6-

407　530.8 and 534.3-532.2 eV assigned to surface adsorbed oxygen (O_{sur}) (O_2^{2-} or O^-) and

408　oxygen species, such as OH. The Bi^{3+}/TiO_2 and Bi_2O_3-N/TiO_2 displayed a higher BE

409　of lattice oxygen, indicating that e^- transfer between TiO_2 and Bi_2O_3. Moreover, the

410　amount of O_{sur} could be increased due to Bi doping. The above measurements indicated

411　the charge transfer between Ti, Bi and O occurring with Bi doping.

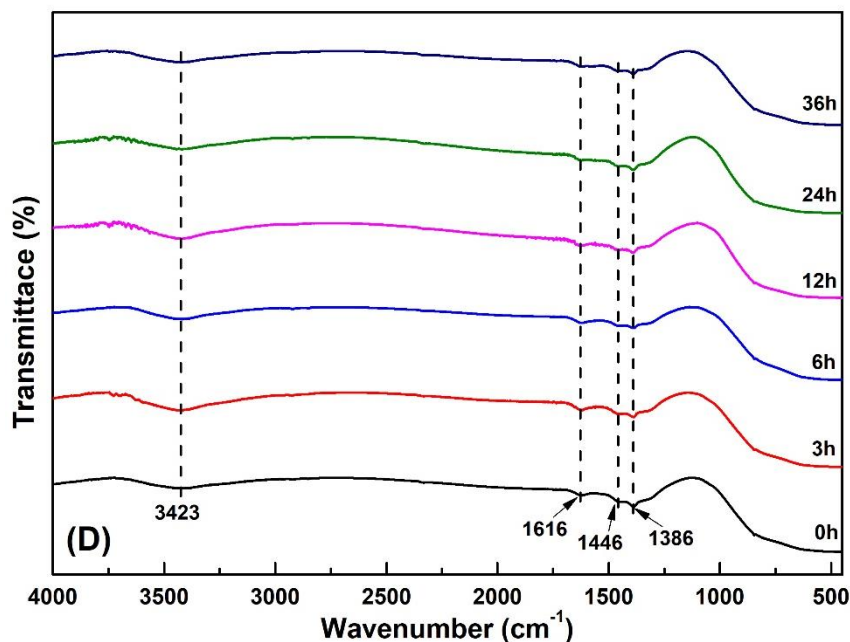412　*3.8 In-situ DRIFTS and IR spectral characteristics*

413

414

415

Base on the In-situ DRIFTS spectra of Bi^{3+}/TiO_2 and Bi_2O_3-N/TiO_2, as shown in Fig. 8A) and Fig. 8(B), upon exposure to a mixed flow of HCHO/O_2 (1.05 ± 0.05 mg/m^3) with different reaction time (0, 3, 6, 12, 24, and 36h) and different bands, such as 591, 1063, 1160, 1237, 1315 cm^{-1} and others could be observed. According to references [1, 2, 8, 9, 14, 42], as for Bi^{3+}/TiO_2, the bands at 591 and 1315 cm^{-1} of Bi^{3+}/TiO_2 can be assigned to the asymmetric stretching vibration of Ti-O-Ti and stretching vibration of Ti-O, respectively [42]. The bending vibration of water at ca. 1611 cm^{-1} and the characteristic bands of molecularly adsorbed HCHO at 1063 cm^{-1} were found in the Bi^{3+}/TiO_2 [14]. The band at 1348 and weak bands at 2822 and 2975 cm^{-1} were attributed to the symmetric v_s(COO) and v_s(CH) stretching of formate [1]. In addition, a broad negative band at ca. 1237 and 1452 cm^{-1} were ascribed to v_s(CH$_2$) and δ(CH$_2$) vibration of dioxymethylene (DOM) [2]. The results implied that formate and DOM species were the main intermediates for photocatalytic oxidation of HCHO. As for Bi_2O_3-N/TiO_2 (Fig. 8(B)), the characteristic bands with different reaction time were almost the same as Bi_2O_3-N/TiO_2(0h) without significant changing. The bending vibration of H_2O at 1618 cm^{-1} and the characteristic bands of molecularly adsorbed HCHO at 1058 cm^{-1} were also discovered. Meanwhile, the bands at 1386, 2848 and 2985 cm^{-1} were also ascribed

436 to the symmetric $v_s(COO)$ and $v_s(CH)$ stretching of formate. With the prolonging

437 reaction time, the band at 1618 cm^{-1} corresponding to the bending vibration of OH^- in

438 water adsorbed decreased and the band at 1710 cm^{-1} assigned to the $v(CO)$ vibration

439 mode of HCHO emerged.

440 The analysis of water absorption and surface hydroxyl showed the IR spectrum of

441 Bi^{3+}/TiO_2 and Bi_2O_3-N/TiO_2 (Fig. 8(C) and Fig. 8(D)). The results seemed to no

442 significant of water absorption and surface hydroxyl change with the reaction time. The

443 stretching vibration at ca. 3423 cm^{-1} corresponded to the hydroxyl group and the

444 bending vibration at ca. 1616 cm^{-1} was attributed to OH- from the adsorption of H_2O.

445 However, Bi^{3+}/TiO_2 exhibited markedly higher H_2O adsorption than Bi_2O_3-N/TiO_2. In

446 addition, the performance of H_2O adsorption could be increased with reaction time, and

447 thus it displayed a higher activity for HCHO oxidation. Due to the inadequate

448 photocatalytic oxidation of HCHO at 3-36h, two absorption bands at ca. 1413 cm^{-1} and

449 2906 cm^{-1} suited to the symmetric or other C–H orientations stretching vibration of

450 formate ($V_s (COO^-)$) were detected. Furthermore, the bands appearing at around 2334

451 cm^{-1}, 1386 cm^{-1}, and 1446 cm^{-1} can be assigned to the stretching or bending vibration

452 of C-O ($V_s (HCO_3^-)$) and $\delta(CH_2)$ vibration of dioxymethylene (DOM) due to the

453 photocatalytic oxidation reaction. The above results confirmed the presence of surface

454 hydroxyls (OH^-) in the structure of these two samples and revealed that the importance

455 of surface hydroxyls on HCHO degradation, especially for Bi^{3+}/TiO_2. These adsorbed

456 H_2O and OH^- are crucial to improve the activity for HCHO oxidation due to their

457 reaction with the photogenerated hole on the surface and the formation of hydroxyl

458 radicals. As the above data of In-situ DRIFTS and IR and reported in literatures [1, 2, 8, 9,

459 14, 42, 43, 44], HCHO was degraded into dioxymethylene (DOM) at first, and then further

460 into formate and carbonate, then finally desorbs as CO_2.

461 *3.9 EPR spectroscopy*

462 To understand the roles of reactive oxygen species such as $^•O_2^-$ and •OH in the

463 photocatalytic process, EPR technique was used to detect the characteristics and active

464 radicals in the samples. As shown in Fig. 9, the value of g=2.003 was ascribed to the

465 paramagnetic characteristic value of $^•O_2^-$ [45], and the value of paramagnetic

466 characteristic could be increased by Bi^{3+} doping with TiO_2. Bi^{3+}/TiO_2 displayed the

467 highest amount of $\cdot O_2^-$, followed by TiO_2, Bi_2O_3-N/TiO_2, and Bi_2O_3. The results showed

468 that the types and amount of Bi doping played an important role in the change of $\cdot O_2^-$

469 concentration. When Bi_2O_3 doped in TiO_2, some of Bi_2O_3 exposed as an electrically

470 charged composite centre, which prevented some e^- from being trapped by oxygen

471 vacancies. The reduce of charged oxygen vacancies resulted in the reduction of the

472 amount of $\cdot O_2^-$ [29]. Therefore, when the amount of $\cdot O_2^-$ decreased, the peak strength on

473 the paramagnetic characteristic of $\cdot O_2^-$ and the activity decreased, which was consistent
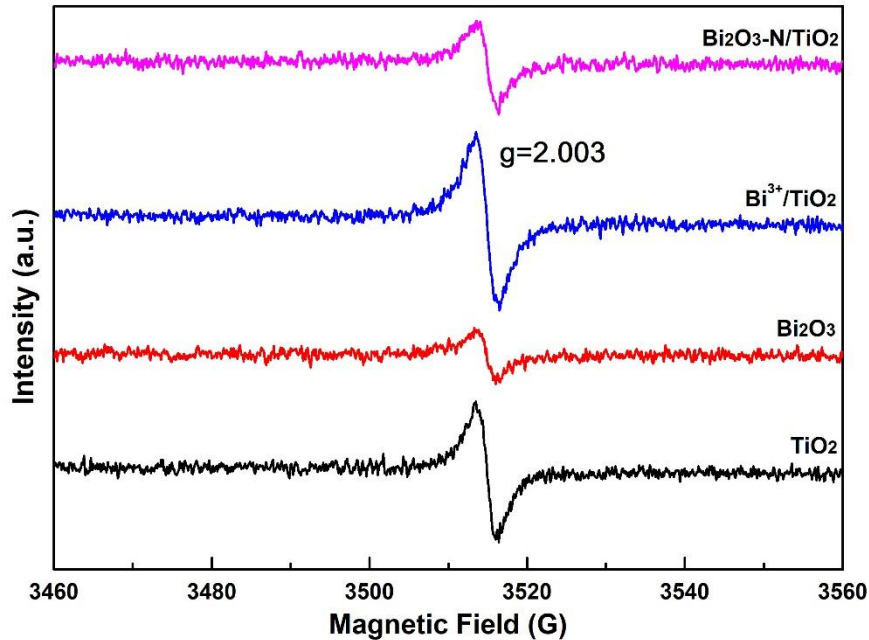
474 with the results of photocatalytic oxidation of HCHO.

475

476 Fig. 9. EPR spectra of different types of TiO_2, Bi_2O_3, and Bi-doped TiO_2 catalysts

477 *3.10 Mechanisms for photocatalytic oxidation of HCHO*

478 Depending on the structure of Bi-doped TiO_2, particularly for Bi^{3+}/TiO_2, the structure

479 of heterojunction, identified as $Bi_4Ti_3O_4$ and TiO_2, could promote efficient charge

480 separation, with the consequence of reducing the recombination of photogenerated e^-

481 and h^+ (Fig. 10). Gan et al. found UV-vis DRS, the E_{bg} for $Bi_4Ti_3O_4$ and TiO_2 were

482 about 2.91 eV and 3.1 eV [46]. Therefore, the E_{cb} and E_{vb} for $Bi_4Ti_3O_4$ and TiO_2 were

483 calculated as -0.41 eV, -0.12 eV, 2.50 eV and 2.98 eV, respectively. Because the E_{cb} of

484 TiO_2 was lower than $Bi_4Ti_3O_4$, the photogenerated e^- could be moved easily from

485 $Bi_4Ti_3O_4$ to TiO_2. The holes transferred in the opposite direction and thus depressed the

486 recombination of e$^-$ and h$^+$. Moreover, the formation of formate species (2822 and 2975

487 cm^{-1}) and dioxymethylene (1237 and 1452 cm^{-1}), ascribed to the results of in-situ

488 DRIFTS spectra, could be found clearly in the Bi^{3+}/TiO$_2$. These two kinds of species,

489 identified as by-products of photocatalytic oxidation, could also be observed by IR

490 spectrum. On the other hand, the weak band at 1710 cm^{-1} corresponding to the v(CO)

491 vibration of HCHO could be observed on the surface of catalysts. More importantly,

492 the intensity of stretching vibration at ca. 3423 cm^{-1} assigned to the hydroxyl group

493 decreased with the extension of reaction time.

494 According to the above investigations, the adsorption of HCHO on the surface was the

495 first step in the catalytic reaction. Bi^{3+}/TiO$_2$ was activated by the visible light and the

496 photogenerated e$^-$ and h$^+$ could be transferred by the heterojunction structure. Then,

497 these e$^-$ can react with O$_2$ to generate superoxide radical anion ($\cdot$O$_2^-$), which can oxidize

498 HCHO into the DOM and formate species. The formate can further break up into CO

499 and H$_2$O, and CO could be further oxidized to CO$_2$ [2, 47]. Another possible pathway is

500 that these photogenerated holes can be combined with OH$^-$ or H$_2$O to generate hydroxyl

501 radical ($\cdot$OH), which could directly oxidize HCHO or formate into CO$_2$ and H$_2$O and
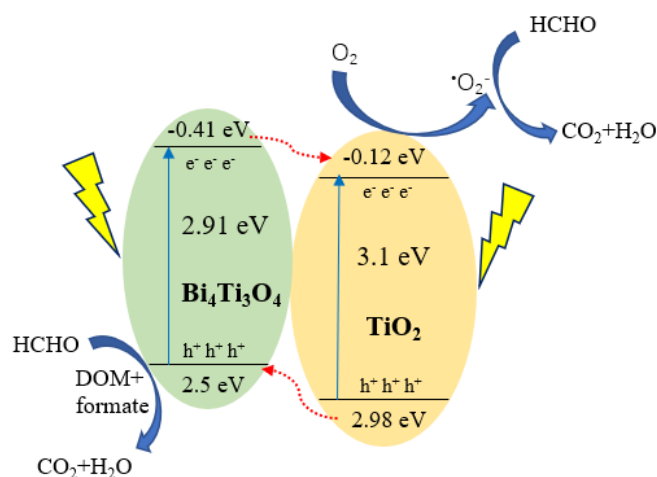
502 tackle the environmental pollution [48, 49].

503

504 Fig. 10. Proposed electron–hole pair separation in the Bi^{3+}/TiO$_2$ composites under visible
505 irradiation

506 **4. Conclusions**

507 In this study, a serious of Bi-doped TiO$_2$ catalysts were synthesized by sol   using the

508 hydrothermal method, and then promoted for the photocatalytic degradation of HCHO

509 under visible light irradiation and ambient temperature. Compared with pure TiO_2 and

510 Bi_2O_3, photocatalytic oxidation of HCHO can be further improved by the Bi-doped

511 TiO_2 catalysts, especially Bi^{3+}/TiO_2. According to the investigation of characterization,

512 it could be observed that the excess Bi_2O_3 doping into TiO_2 catalysts, such as Bi_2O_3-

513 N/TiO_2 and Bi_2O_3-C/TiO_2, formed a mixed oxides with Bi_2O_3 and $Bi_4Ti_3O_{12}$, and they

514 were disadvantage to enhance the activity. However, Bi^{3+}/TiO_2 composed of TiO_2 and

515 $Bi_4Ti_3O_{12}$ displayed a higher activity and remained good stability for HCHO oxidation.

516 It was worth mention that Bi^{3+}/TiO_2 didn't have the lowest binding energy, but it

517 displayed a lower PL intensity. The highest activity mainly depends on the uniform

518 particulates, high surface areas, and the great interaction between TiO_2 and $Bi_4Ti_3O_{12}$

519 via charge transfer.

520 In summary, this study demonstrated that HCHO can be effectively oxidized to 0.058

521 mg/m^3 (94.7%) at visible light excitation within 36 h. The heterogeneous catalysts

522 with TiO_2 and $Bi_4Ti_3O_{12}$ were the main critical factor to degrade gaseous organic

523 pollutants. The results made new contribution for a better understanding of the existing

524 state of Bi in the TiO_2 crystal.

525

537

References

[1] F. Liu, S.P. Rong, P.Y. Zhang, L.L. Gao. Appl. Catal. B 235 (2018) 158.

[2] D. Sun, S. Wageh, A.A. Al-Ghamdi, Y. Le, J.G. Yu, C.J. Jiang. Appl. Surf. Sci. 466 (2019) 301.

[3] V. Binas, V. Stefanopoulos, G. Kiriakidis, P. Papagiannakopoulos. J. Mater. 5 (2019) 56.

[4] A. Okawa, R. Yoshida, T. Isozaki, Y. Shigesato, Y. Matsushita, T. Suzuki. Catal. Commun. 100 (2017) 1.

[5] X.A. Dong, W. Cui, H. Wang, J.Y. Li, Y.J. Sun, H.Q. Wang, Y.X. Zhang, H.W. Huang, F. Dong. Sci. Bull. 64 (2019) 669.

[6] J.Y. Li, X.A. Dong, G. Zhang, W. Cui, W.L. Cen, Z.B. Wu, S. C. Lee, F. Dong. J. Mater. Chem. A 7 (2019) 3366.

[7] Z. Zhang, J. Huang, H.Q. Xia, Q.G. Dai, Y.F. Gu, Y.J. Lao, X.Y. Wang. J. Catal. 360 (2018) 277.

[8] Z.X. Yan, Z.H. Xu, Z.H. Yang, L. Yue, L.Y. Huang. Appl. Surf. Sci. 467 (2019) 277.

[9] Y. Zhang, M.X. Chen, Z.X. Zhang, Z. Jiang, W.F. Shangguan, H. Einaga. Catal. Today. 327 (2019) 323.

[10] D. Kibanova, M. Sleiman, J. Cervini-Silva, H. Destaillats. J. Hazard. Mater. 211 (2012) 233.

[11] X.Q. Deng, J.L. Liu, X.S. Li, B. Zhu, X.B. Zhu, A.M. Zhu. Catal. Today. 281 (2017) 630.

[12] J.Y. Li, W. Cui, P. Chen, X.A. Dong, Y.H. Chu, J.P. Sheng, Y.X. Zhang, Z.M. Wang, F. Dong. Appl. Catal. B 260 (2020) 118130.

[13] X.S. Li, X.Y. Ma, J.L. Liu, Z.G. Sun, B. Zhu, A.M. Zhu. Catal. Today. 337 (2019) 132.

[14] S.Y. Huang, B. Cheng, J.G. Yu, C.J. Jiang. ACS Sustain. Chem. Eng. 6 (2018) 12481.

[15] G.K. Zhang, Q. Xiong, W. Xu, S. Guo. Appl. Clay. Sci. 102 (2014) 231.

[16] M. Malayeri, F. Haghighat, C.S. Lee. Build. Environ. 154 (2019) 309.

[17] G.X. Zhang, Z.M. Sun, Y.W. Duan, R.X. Ma, S.L. Zheng. Appl. Surf. Sci. 412 (2017) 105.

[18] X. Li, X.R. Qian, X.H. An, J.W. Huang. Appl. Surf. Sci. 487 (2019) 1262.

[19] R.F. Liu, W.B. Li, A.Y. Peng. Appl. Surf. Sci. 427 (2018) 608.

[20] M. He, J. Ji, B.Y. Liu, H.B. Huang. Appl. Surf. Sci. 473 (2019) 934.

[21] T. Ohno, M. Akiyoshi, T. Umebayashi, K. Asai, T. Mitsui, M. Matsumura. Appl. Catal. A 265 (2004) 115.

[22] X.Y. Pan, Y.J Xu. J. Phys. Chem. C. 117 (2013) 17996.

[23] J. Li, M. Zhang, Q.Y. Li, J.J. Yang. Appl. Surf. Sci. 391 (2017) 184.

[24] C. Huang, Y. Ding, Y.W. Chen, P. Li, S.B. Shen. J. Environ. Sci. 60 (2017) 61.

[25] S.H. Liu, W.X. Lin. J. Photoch. Photobio. A 378 (2019) 66.

[26] W. Low, V. Boonamnuayvitaya. J. Environ. Manage. 127 (2013) 142.

[27] J.P. Li, D.J. Ren, Z.X. Wu, J. Xu, Y.J. Bao, S. He, Y.H. Chen. J. Colloid. Inter. Sci. 530 (2018) 78.

573 [28] Q. Huang, P. Wang, Y.Z. Fan, Q. Wang. Indoor. Built. Enviro. 26 (2017) 785.

574 [29] Y.F. Huang, Y.L. Wei, J. Wang, D. Luo, L.Q. Fan, J.H. Wu. Appl. Surf. Sci. 423 (2017) 119.

575 [30] Y.B. Liu, G.Q. Zhu, J.Z. Gao, M. Hojamberdiev, R.L. Zhu, X.M. Wei, Q.M. Guo, P. Liu. Appl.
576   Catal. B 200 (2017) 72.

577 [31] S. Murcia-López, M. Hidalgo, J.A. Navío. Appl. Catal. A 404 (2011) 59.

578 [32] B. Benalioua, M. Mansour, A. Bentouami, B. Boury, E.H. Elandaloussi. J. Hazard. Mater. 288
579   (2015) 158.

580 [33] A. Hamdi, A.M. Ferraria, A.M. Botelho Rego, D.P. Conceicao, L.F. Vieira Ferreira, S.
581   Bouattour. J. Mol. Catal. A 380 (2013) 34.

582 [34] L.W. Lu, M.L Lv, D. Wang, G.Liu, X.X. Xu. Appl. Catal. B 200 (2017) 412.

583 [35] J.H. Lee, H. Lee, M.J. Kang. Mater. Lett. 178 (2016) 316.

584 [36] J. Zhu, S.H. Wang, J.G. Wang, D.Q. Zhang. Appl. Catal. B 102 (2011) 120.

585 [37] C.C. Pei, W.W.F. Leung. Appl. Catal. B 174 (2015) 515.

586 [38] J.Z. Wang, H.L. Li, X.R. Yan, C. Qian, Y.J. Xing, S.T. Yang, Z.K. Kang, J.Y. Han, W.X. Gu,
587   H.Y. Yang, F.J. Xiao. J. Alloys. Compounds. 795 (2019) 120.

588 [39] Y. Hu, Y.T. Cao, P.X. Wang, D.Z. Li, W. Chen, Y.H. He, X.Z. Fu, Y. Shao, Y. Zhang. Appl.
589   Catal. B 125 (2012) 294.

590 [40] T.V.L. Thejaswini, D. Prabhakaran, M.A. Maheswari. J. Environ. Chem. Eng. 4 (2016) 1308.

591 [41] Q. Huang, Q. Wang, T. Tao, Y.X. Zhao, P. Wang, Z.Y. Ding, M.D. Chen. Environ. Technol. 40
592   (2019) 1937.

593 [42] H.S. Zuo, J. Sun, K.J. Deng, R. Su. Chem. Eng. Technol. 30 (2007) 577.

594 [43]P. Liu, G.L. Wei, H.P. He, X.L. Liang, H.L. Chen, Y.F. Xi, J.X. Zhu. Appl. Surf. Sci. 464   (2019)
595   287.

596 [44] P. Liu, G.L. Wei, X.L. Liang, D. Chen, H.P. He, T.H. Chen, Y.F. Xi, H.L. Chen, D.H. Han, J.X.
597   Zhu. Appl. Clay. Sci. 161 (2018) 265.

598 [45] C.P. Kumar, N.O. Gopal, T.C. Wang, M.S. Wong, S.C. Ke. J. Phy. Chem. B 110 (2006) 5223.

599 [46] H.H. Gan, F.T. Yi, H.N. Zhang, Y.X. Qian, H.X. Jin, K.F. Zhang. Chinese. J. Chem. Eng. 26
600   (2018) 2628.

601 [47] Y. Ma, G.K. Zhang. Chem. Eng. J. 288 (2016) 70.

602 [48]. H. Yang, X. Huang, J.R. Thompson, R.J. Flower. Science 347 (2015) 834.

603 [49]. H. Yang. Nature 509 (2014) 535.